Skeleton-Based 3D Femur Shape Analysis System Using Maximum-Minimum Centre Approach

SEOW HUI SAW[1], **BYUNG-GOOK LEE**[2], **AND HONG TAT EWE**[3], (Senior Member, IEEE)
[1]Department of Computer Science, Faculty of Information and Communication Technology, Universiti Tunku Abdul Rahman, Kampar, Perak 31900, Malaysia
[2]Division of Computer Engineering, Dongseo University, Busan 47011, South Korea
[3]Department of Electrical and Electronic Engineering, Lee Kong Chian Faculty of Engineering and Science, Universiti Tunku Abdul Rahman, Cheras, Kajang, Selangor 43000, Malaysia

Corresponding author: Seow Hui Saw (shsaw@utar.edu.my)

ABSTRACT Femoral shaft fractures are correlated with frequent morbidity and mortality. It is a major musculoskeletal disorder caused by tremendous force applied to the femur. One of the most common surgical treatments for fixation is intramedullary nailing (IM), which utilises a specially designed metal rod and screws to be implanted into the medullary canal. However, severe bowing of the femur can result in a mismatch between the IM nail and the alignment of the femur. Such mismatch is a risk factor for anterior cortical perforation off the distal femur with subtrochanteric fractures and leg length discrepancy with fractures of the femoral shaft. Therefore, accurate three-dimensional (3D) preoperative planning is mandatory to facilitate the implant's design based on the obtained geometric data, especially for the fractured bowed femur. This paper presents an automatic 3D femur shape analysis system (3D-FSA) based on the extracted skeleton of each individual patient to provide an accurate 3D preoperative simulation. The structure of the 3D femur was generated using a set of computed tomography (CT) images. By using the maximum-minimum centre approach for skeletonization, significant geometric and topological information was captured. The proposed approach can potentially assist in implant measurements.

INDEX TERMS CT images, femoral shaft fractures, intramedullary nail, internal fixation surgery, measurement analysis, medial axis transform, orthopaedics, 3D mesh, 3D skeletonization.

I. INTRODUCTION

Three-dimensional (3D) skeletonization is the process of generating a skeleton, sometimes called the curve skeleton. It provides an alternative for capturing the inner structure of an overall complex 3D mesh. These computed skeletons consist of significant geometric and topological information that are used extensively to produce segmentation for various analyses and visualisations in medical imaging [1], robotics [2], reverse engineering [3] and video surveillance systems [4].

For decades, many research efforts have focused on finding an optimal approach for generating skeletons from these digital meshes. These approaches are divided into three main categories: (*i*) Medial Axis (MA) [5], [6], (*ii*) Reeb Graph [7] and (*iii*) Geometric Contraction [8]. This study mainly focused

The associate editor coordinating the review of this manuscript and approving it for publication was Charalambos Poullis.

on the medial axis, which is a set of curves defined as the locus of the centres of balls that are tangent to and maximally inscribed in the 3D mesh, that is, such balls contained in the mesh are tangential to three or more points of the mesh without crossing the boundaries. Hence, the medial axis transform (MAT) is a combination of the medial axis and the radius function that determines the maximally inscribed balls, and the medial axis skeleton is generated.

The concept of the medial axis was first presented by Blum [9] for biological shape analysis, and was applied in this study. Since it is difficult to compute MAT accurately, several strategies are used to construct a skeleton that approximates the medial axis for different purposes, such as Voronoi diagrams [6], [10], 3D voxel grids [11], [12] and others. These strategies are common and difficult to implement in skeleton representations.

In this study, the maximum-minimum centre approach is proposed for the skeleton extraction. This method is an

automatic and straightforward method that can be used, especially on the human femur. Although the development of the skeletonization is relatively well established in medical research, and skeleton computation in 3D human femurs is relatively unexplored in the study of orthopaedics.

The human femur is the longest, heaviest and strongest bone in the human body. Different kinds of trauma with many forces can result bone damage, such as in some motor vehicle accidents or motorcycle crashes. This can also occur in a lower-force accidents, such as falls from slippery floors, and ladder landing on foot among the older people due to their weaker bones or osteoporosis. There are usually two types of treatments for femoral fractures: nonsurgical and the surgical. Nonsurgical treatment requires only a cast to heal. This is mostly applicable to very young children. In contrast, surgical treatment requires surgery to repair and heal the broken bones within 24 to 48 hours.

Open reduction and internal fixation (ORIF) is a surgical treatment that consists of two procedures performed under anaesthesia: open reduction and internal fixation [13], [14]. The first step is open reduction, in which the orthopaedic surgeon cuts the skin and adjusts the fractured bone to the normal position. The second part is internal fixation, where the bone fragments are held together with fixation devices such as plates, screws, stainless steel pins and wires until bone union [15], [16].

IM is the most common surgical treatment for certain diaphyseal fractures of the femur [17]. During this procedure, a specially designed metal rod, also known as an intramedullary nail (IM nail), is inserted into the medullary canal and passes across the fractured bone to maintain its position (Fig. 1). Finally, screws are placed above and below the fracture to hold the femur in the correct alignment while the bone heals [18].

Nonetheless, orthopaedic surgeons often encounter severe problems such as iatrogenic fractures and complications during implant insertion due to exaggerated femoral bowing and narrowing of the diameter of the medullary canal [19]–[23]. Severe bowing of the femur can result from a mismatch between the IM nail and the alignment of the femur. This mismatch occurs because most of the implants are designed for the femur, which does match the exaggerated bowing. Such mismatch is a risk factor for anterior cortical perforation off the distal femur with subtrochanteric fractures, and leg length discrepancy (LLD) with fractures of the femoral shaft. LLD after IM nailing of femoral shaft fractures is common and is reported in 20 to 30 % of cases [24]. Several techniques were proposed in [25]–[28] to prevent intraoperative LLD during femoral fracture fixation. In addition, [29], [30] measured the LLD for several patients who had treated their femoral shaft fracture with IM nails for early intervention and repeat surgery.

Therefore, several morphological studies have been conducted on the differences in the magnitude of femoral bowing among the Asian population [31]–[34] and Western populations [35]–[40]. In addition, the other significant parameters

FIGURE 1. An example of a specially designed metal rod, also known as an intramedullary nail (IM nail).

of the human femur, such as femoral length, diameter of medullary canal, radius of curvature (ROC), femur length and etc., were assessed using either roentgenogram [41]–[43], computed tomography (CT) [34], [44]–[46], 3D spaces [32], [33], [47]–[50] or 3D printed models [21]. These parameters obtained from all walks of life, various races and ages are used as a reliable frame of reference during the preoperative templating and preoperative design of custom-made implant devices [22].

Femoral bowing can be determined by measuring of the angulation between the proximal and distal quarters of the femoral diaphysis, and the cut-off value was defined between 5.25° and 7° [38], [51], [52]. Thus, a preoperative planning template in orthopaedic surgery is an essential prerequisite to estimate the correct nail diameter and length for the success of the procedures. Conventionally, the detailed surgical plan and measurement are written down as blueprints and performed on hardcopy radiographs using various methods. This practice has become less practical because of a lack of consistency in radiographic magnification [53] and the rapid development of computer-aided design (CAD) software for deriving 3D meshes from reconstructed lateral radiographs or images using CT images [33].

This paper presents an accurate and automatic 3D preoperative simulation called 3D-FSA that produces a skeleton of the 3D femur using the maximum-minimum centre approach for the analysis of femoral shaft geometry, which focuses on the femoral bowing and femoral width [50]. These parameters are very useful for orthopaedics to accurately perform preoperative evaluations and engineers in developing a new intramedullary nailing system.

II. ALGORITHM OVERVIEW
There are four main modules in our proposed approach, as illustrated in Fig. 2. It begins with the preprocessing that takes individual snapshots of the individual human femur into a set of cross-sectional images, which is also known as CT imaging. These images were approved by the Institutional Review Board of the participating centre and saved in digital imaging and communications in medical format [50]. They were then imported into a 3D modelling software (AVIEW Modeller; Coreline Soft, Seoul, South Korea [54]) to produce 3D samplings of anatomical elements for the human femur. With the use of reconstruction and parametrisation from such datasets, structured data can be obtained to form a 3D mesh representing both the bone surface and corticocancellous interface in the 3D-FSA, as shown in Fig. 3.

The structured data used in this study were presented in *.obj* format, as explained in Section III. Once the 3D femur is constructed, its skeleton is obtained in the 3D skeletonization module (explained in Section IV) using the maximum-minimum centre approach. Thus, the obtained skeleton was used to perform the necessary shape analysis due to its compact representation of the femur. Detailed descriptions of each module are presented in Sections III and IV.

III. 3D FEMUR CONSTRUCTION

The 3D-FSA is a shape analysis system that specialises in representing and manipulating triangulated surfaces for both the human bone and the corticocancellous interface using the maximum-minimum centre approach (Section IV). This system provides a support platform for 3D femur formation that handles meshes in *.obj* file format, as shown in Fig. 3.

The *.obj* file format is a geometry definition file format that is equipped with all the necessary data formats, namely, the position of each vertex, the respective normal value for each vertex that represents the reflection of lighting or Phong shading, and the list of vertices that define the faces for the 3D femur; thus, the analysis and experiment for this research became more accurate, consistent and robust. Illustrations of the 3D femur in the view of vertices are shown in Fig. 3(a), and in the faces view can be seen in Fig. 3(b).

According to [55], *.obj* is a crucial file formats in both 3D printing and 3D graphics applications. It was originally created by Wavefront Technologies for its advanced visualisation application to store geometric objects composed of lines, polygons, and freeform curves and surfaces. In addition, the colour and texture information can be stored in this file format too. Nevertheless, no scene information, such as the light position or animations, can be stored in it.

The *.obj* file format is a simple and open format with wide export and import support among computer aided design (CAD) software. For example, the Autodesk 3ds Max is used to convert the rendered 3D mesh into *.obj* file format and read it using the Notepad in Windows or TextEdit in MacOS. Hence, *.obj* has become famous as a file format for 3D meshes.

IV. 3D SKELETONIZATION

This is the most significant module in our algorithm after Section III, which calculates the MAT and produces a skeleton from the 3D femur. MAT was introduced by Blum [9] and is mainly composed of two properties: the medial axis (MA) and the radius function (refer to (1)).

Let Ω be a connected bounded domain in $\mathbb{R}$ with $n-$dimensions, and let B to be the loci of all maximal inscribed disks that meet two or more boundary points without crossing any of the boundaries in Ω. We define MA, denoted by $MA(\Omega)$, as the set of centres of the disks in B [56] as written in (2).

Each vertex p in the $MA(\Omega)$ is defined as a set of the pairs consisting of the centre and the radius r of the disks in

$B_r(p) \in B$, which forms the medial circle, and the volume is enclosed by the surface in Ω, which is exactly the union of these circles, as presented in (2).

$$MAT(\Omega) = \{(p, r) \in \mathbb{R}^n \times \mathbb{R} | B_r(p)$$
$$\text{is maximal ball in } \Omega\} \tag{1}$$
$$MA(\Omega) = \{p \in \mathbb{R}^n | r \geq 0 \quad \text{s.t. } (p, r) \in MAT(\Omega)\} \tag{2}$$

Therefore, to obtain the skeleton of the 3D femur, we determined the maximum radius of the circle that is well suited for each slice of the irregular inner 3D femur. Before further explanation, we review some basic facts regarding graphs in the context of 3D skeletonization. A bidirectional weighted graph $G = \{V, E\}$ consists of a set of vertices V and a set of bidirectional edges E that connect them. The 3D femur is composed of a large number of faces F that are made of three connected edges each, or in other words, a triangle.

In this study, four processes were involved, as depicted in Fig. 4, to compute a reliable and consistent skeleton from a 3D femur. A more detailed explanation is provided in the following subsections.

A. AXIS ADJUSTMENT AND FEATURE DETECTION

At the beginning of the program, this process involves detecting and recognising the distinctive features of the 3D femur. It examines every vertex to determine the position of the distal femur (the area of the leg just above the knee joint [18]) and proximal femur (including the femoral head, neck and the region 5-cm distal to the lesser trochanter [57]).

Using the obtained measurements, the dimensions, including the width, height and depth of the 3D femur, were determined. Moreover, the (x, y, z)-axes are modelled in the coordinate system of 3D-FSA using the appropriate geometric transformations, such as translation. Fig. 5 illustrates the outcomes of this process.

In addition, two bounding boxes that were drawn as rectangles (*pink* colour), as shown in Fig. 5, were constructed. These bounding boxes are served as the indicators of the beginning (the distal femur) and ending (the proximal femur) bases for the 3D femur.

The green cylindrical shape made of two separate circles with the calculated distance h, between these circles is defined as the sliding window (depicted in Fig. 6). The value h can vary depending on the user's decision.

The purpose of this sliding window is to slide over the entire 3D femur from the beginning to the end to capture and slice different portions.

Each slice that is captured by the sliding window is used to collect the adjacent faces within that portion, as shown in brown in Fig. 6, and perform some calculations in Sections IV-B and IV-C.

B. MAXIMUM-MINIMUM CENTRE APPROACH

Fig. 7 shows the steps involved in this approach. It begins with the sliding process at position $z-$coordinate, together with the defined sliding window s, and the computed
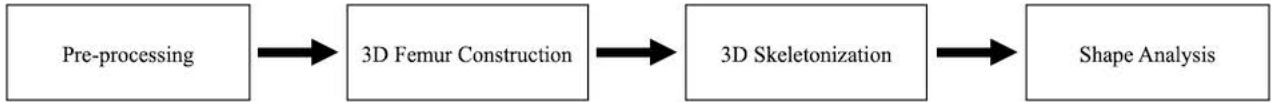
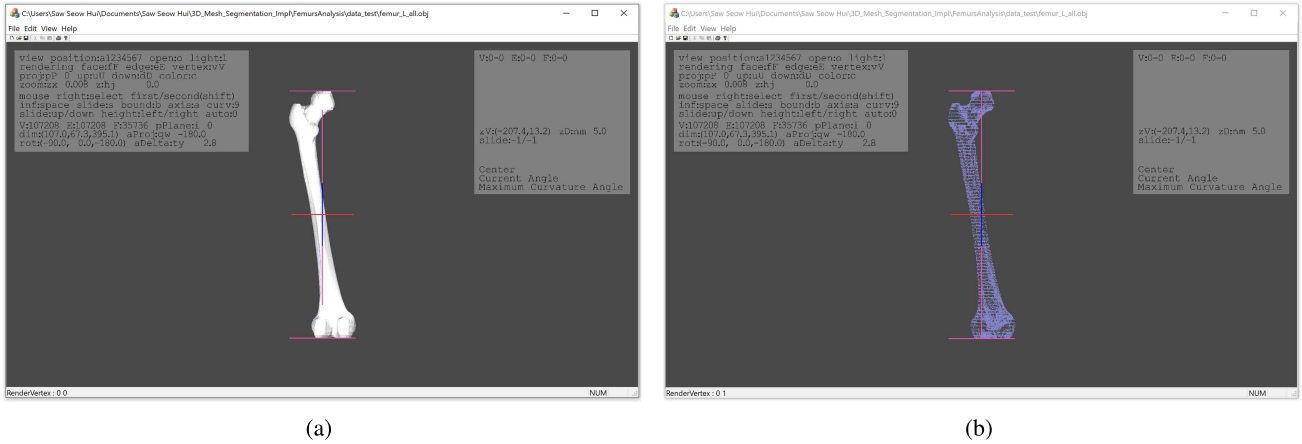**FIGURE 2.** Overview of the proposed algorithm.

FIGURE 3. The interface of the 3D-FSA. (a) 3D left femur in faces view, and (b) 3D right femur in vertices view.
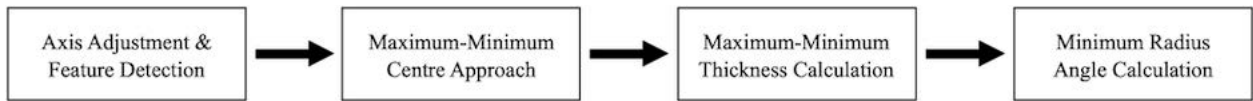

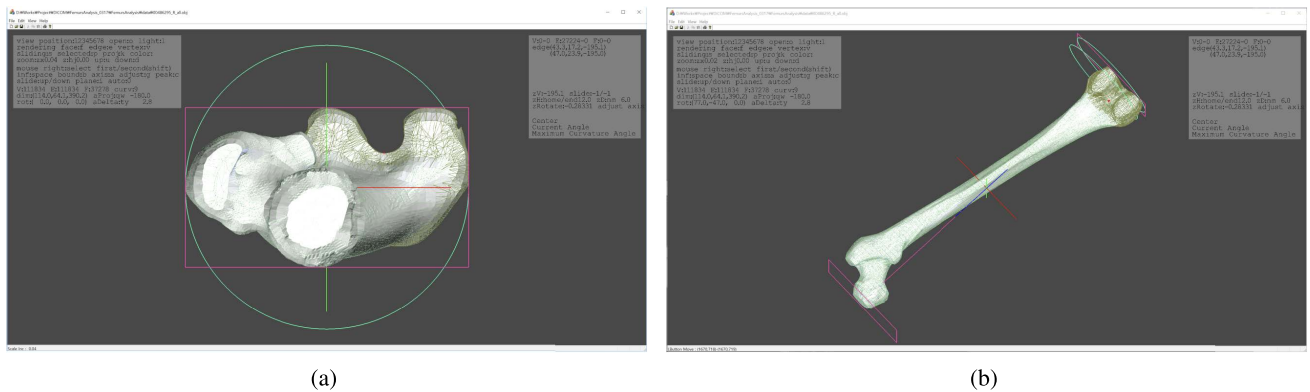**FIGURE 4.** The involved processes for 3D skeletonization.

FIGURE 5. The calculation of the dimensions and adjustment for the axes in three dimensions based on the size of the 3D femur. Left femur: (a) The $(x, y) - axis$ adjustment, bounding box (*pink in colour*) and the sliding window (*green in colour*) calculated by the width and height of the left femur, (b) The $z - axis$ adjustment extracted from the length of the left femur.

distance h. During this process, the vertices v_z within this selected portion from z to $z + h$ are collected and added to V_s (refer to (3)).

Then, the faces adjacent to each vertex in V_s are captured and stored in F_s with a total number of m faces. We take the advantage of the Lindstrom and Turk approach [58], which introduces the simplex operators for fast and memory-efficient 3D mesh simplification. The equation is denoted in (4) to acquire these adjacent faces. Fig. 6 illustrates the

sliding window (cylinder shape in green) and the adjacent faces within the selected portion (highlighted faces in brown).

$$V_s = \{v : v_z \in (z, z + h)\}$$
$$where \ v = (v_x, v_y, v_z) \in R^3, \quad s = (z, z + h). \quad (3)$$
$$F_s = \lceil \lceil V_s \rceil \rceil = \{f_i\}_{i=0}^m. \quad (4)$$

With the acquired adjacent faces in F_s, the area $A(f_i)$ for each face i in F_s and its centroid $\bar{f}_i$ are calculated using
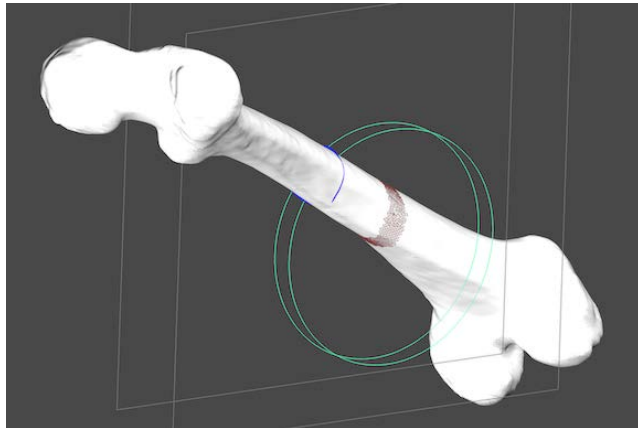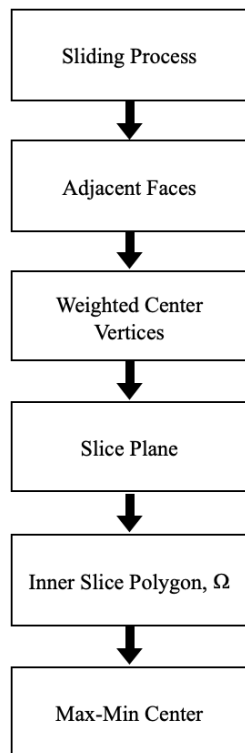
the cross product and formula in (5), respectively. This is followed by multiplying both calculated values, to derive the weighted area for each face i using (6). The weighted normal is also derived by multiplying the face area $A(f_i)$ together with the face normal $N(f_i)$, as defined in (7).

$$\bar{f}_i = \frac{1}{3}\sum_{i=0}^{2} v_i. \qquad (5)$$

$$Weighted\ Area = A(f_i)\bar{f}_i$$
$$where\ A(f_i) = area\ of\ a\ face\ f_i,\ and$$

$$\bar{f}_i = centroid\ of\ a\ face\ f_i \qquad (6)$$

$$Weighted\ Normal = A(f_i)N(f_i)$$
$$where\ N(f_i) = normal\ of\ a\ face\ f_i \qquad (7)$$

Then, the weighted centre vertices $\bar{F}_s$ as defined in (8), for all the faces in F_s are derived by dividing the accumulation of the weighted areas in (6) and the accumulation of the areas A_s. Moreover, the accumulation of the weighted normal for all the faces in F_s is calculated to be used as the numerator of the fraction, as denoted in (9). The values obtained from (8) and (9) are the average of the areas and the common orientation of the faces in F_s, respectively.

$$\bar{F}_s = \frac{1}{A_s}\sum_{i=0}^{m} A(f_i)\bar{f}_i$$
$$where\ A_s = \sum_{i=0}^{m} A(f_i),\ A(f_i) = area\ of\ a\ triangle\ f_i,\ and$$
$$\bar{f}_i = centroid\ of\ a\ triangle\ f_i. \qquad (8)$$
$$\bar{N}_s = \frac{1}{m}\sum_{i=0}^{m} A(f_i)N(f_i)$$
$$where\ m = the\ total\ number\ of\ faces\ in\ f_i. \qquad (9)$$
$$R_s = A(f_i)N(f_i) - \bar{N}_s \qquad (10)$$

The weighted centre vertices $\bar{F}_s$ define the medial axis of the 3D femur, as plotted using small and green spheres in Fig. 9. It defines the loci of all maximal inscribed disks that meet the inner boundary without any overlap, that is, the skeleton, as shown in Fig. 15. In addition, F_s is crucial in finding the thickness of the medullary canal in subsection IV-C and the radius angle calculation in subsection IV-D.

Whereas the weighted normal $\bar{N}_s$ is used to find the residual error rates for the average of the weighted normal as shown in (10). These values are used to derive the equation for the least squares plane fitting, which is then used to render the projection plane in the centre, as illustrated in Fig. 8 (peach in colour).

During the sliding process, the sliding window serves as a slice plane, which slices the 3D femur from the beginning until the end, with a thickness of h, as shown in Fig. 8 (the two green circles). The vertices V_s within this sliding window are all projected onto the formed projection plane.

The blue vertices in the centre as shown in Fig. 8 and Fig. 9, represent the vertices projected from the sliding window during the sliding process. We refer to these projected vertices as the inner slice polygon Ω_s.

The inner slice polygon Ω_s represents the medullary canal of the 3D femur. The explanation of how to find this thickness is explained in Section IV-C.

Finally, the maximum-minimum centre was acquired from the results generated from the weighted centre vertices $\bar{F}_s$ and the maximum-minimum thickness of the medullary canal (Section IV-C) as illustrated in the maximal green circle $B_s(p, r)$ in Fig. 9.
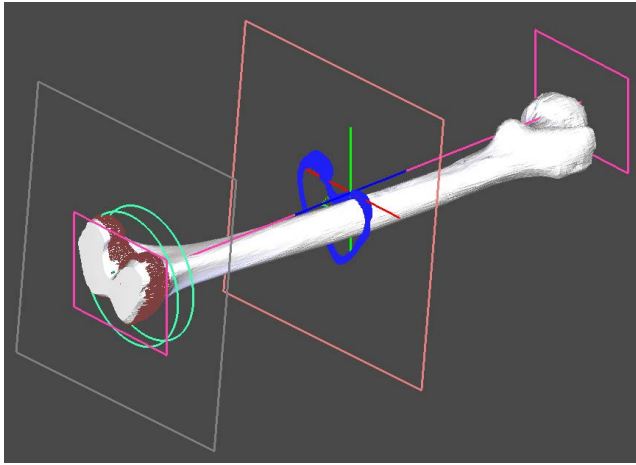
FIGURE 8. The sliding window (2 *green circles*), the slice plane in rectangle shape (*grey in colour*) and the projection plane in rectangle shape that located in the centre (*peach in colour*).
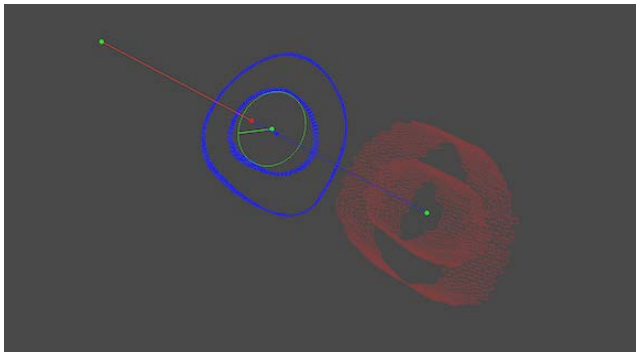

FIGURE 9. Weighted centre vertex (*green vertex*), inner slice polygon Ω_s (*blue vertices*), maximal circle $B_s(p, r)$ (*green circle and line*).

The definition and notation used in this step are summarised as follows:

1) Slice plane: Calculate the weighted average of the face normal
2) Sliding window as base plane: Face normal average.
3) Inner slice polygon Ω_s: Projection face centre to base plane.
4) Max-Min Centre: $B_s(p, r)$ is the maximal circle in Ω_s.

C. MAXIMUM-MINIMUM THICKNESS CALCULATION

The anatomical parameters of the femur, such as the diameter (thickness) of the isthmus and the medullary canal, are significant in the preoperative measurements [19], [33], [59]. To obtain scaled measurements, the diameter (thickness) of both the isthmus and medullary canal was directly obtained by detecting the contours of the 3D femur in this step of the 3D-FSA.

A contour is a representation of a set of linking edges corresponding to a regional boundary [60]. Contours are a useful tools for shape analysis, object detection and recognition. In 3D-FSA, contour N is represented as an ordered

list of vertices that are used to construct the linking edges. Contours 1 and 2 of the medullary canal are defined as illustrated in Fig. 10, with the output produced in Section IV-B, such as the projected plane P, projected weighted centre vertices $P(\bar{F}_s)$, and the inner slice polygon Ω_s.

As shown in Fig. 10, contour 1 is defined as the outer curve of the inner boundary of the medullary canal, and all projected linking vertices a are saved in set A, whereas contour 2 is defined as the outer curve of the inner boundary of the medullary canal, and all projected linking vertices b are saved in set B. The relationship between these sets are depicted in (11).

The diameter (thickness) of the medullary canal was then measured using the instructions provided in Algorithm 1. Starting from vertex $a_i \in A$ of contour 1, we compare it with all vertices in set B of contour 2. In each comparison, only the minimum distance between these values is acquired and saved in $minDist$, as illustrated in Fig. 11(a). This process is repeated until all the vertices $a \in A$ are compared. When vertex $a_i \in A$ is changed in each execution, the maximum value $maxDist$ is selected after a comparison with the acquired $minDist$.

After all the vertices $a \in A$ of contour 1 are examined, the algorithm continues with the vertices $b \in B$ which go through the same comparison process, and the minimum distance $minDist$ is collected. The minimum distance $minDist$ is then compared with the $maxDist$ to obtain the maximum distance of all, as shown in Fig. 11(b).

Three significant variables are generated from this step: 1) c_i, 2) c_j, and 3) $maxDist$. These variables were used to determine the diameter of the medullary canal by finding the closest distance from contours 1 to 2, and the radius r was obtained using (12), which forms the *maximal circle* $B_s(p, r)$ of the 3D femur, as illustrated in Fig. 12.

$$Contour\ 1 : A \in N$$
$$Contour\ 2 : B \in N$$
$$A \cup B = N$$
$$A \cap B = \emptyset \tag{11}$$
$$radius = \sqrt[2]{maxDist} \tag{12}$$

D. MINIMUM RADIUS ANGLE CALCULATION

As defined in [61], any approximate circular radius at any particular point is called the radius of curvature (ROC) of the curve. As we move along the curve, the ROC changes. In differential geometry, the ROC is denoted by R. The *maximal circle* $B_s(p, r)$ and medullary curvatures of 3D femurs are produced in Section IV-C to determine the amount by which the curve derivates itself from being flat to a curve and from a curve back to a line. The ROC is the reciprocal of the curvature.

This is another important preoperative parameter studied by many researchers [19], [21], [33], [33], [34], [42], [46],

FIGURE 10. Contour detection of the medullary canal. Contour 1 indicates the inner curve of the outer boundary, whereas contour 2 indicates the outer curve of the inner boundary. (a) The contours are yet to be rendered. (b) The contours are rendered with green in contour 1 and with tangerine in contour 2. These rendered vertices N, $A \in N$ from contour 1 and vertices $B \in N$ from contour 2 are used to calculate the maximum-minimum thickness of the medullary canal.
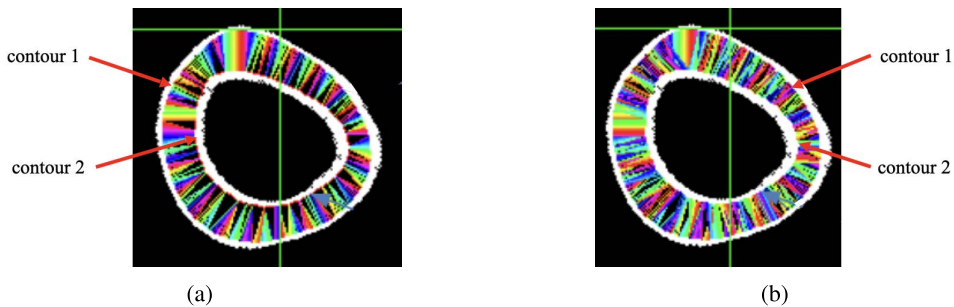

FIGURE 11. The maximum-minimum thickness calculation. (a) Begin with a vertex $a_i \in A$ in contour 1 and compare the distance between vertex $a_i \in A$ and all vertices B in contour 2. The closest distance *minDist* is selected between vertex $a_i \in A$ and vertex $b_i \in B$. (b) Begin with a vertex $b_i \in B$ in contour 2 and compare the distance between vertex $b_i \in B$ and all vertices A in contour 1. The closest distance *minDist* is selected between vertex $b_i \in B$ and vertex $a_i \in A$.
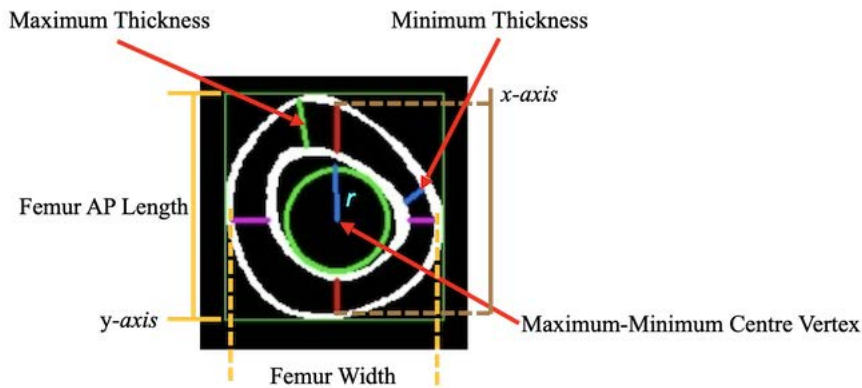

FIGURE 12. The maximal circle $B_S(p, r)$ (green circle) and the radius r, with the diameter (thickness) of medullary canal $= 2r$. These parameters are computed using the approaches described in Sections IV-B and Section IV-C.

[50]–[52], [62]–[68] due to the difference between the curves of the femur and the contemporary femoral nails implicates the inadequacy of the implant design.

Therefore, 3D-FSA provides the computation for finding the curvature of the curve for the 3D Femur as written in Algorithm 2. The basic concept behind this computation is as follows:

"The circle defined by centre (a, b) and radius r will yield the least mean square value for the expression $(x - a)^2 + (y - b)^2 - r^2$ and the circle's curvature will be $\frac{1}{r}$".

Fig. 13 demonstrates two examples for the involved range of this calculation with various starting indices but similar ending indices. Additionally, Fig. 14 shows the projected vertices used for the calculation of the minimum radius of

Algorithm 1 Algorithm for Maximum-Minimum Thickness Measurement of Medullary Canal

Input:
    Projected Plane P;
    Projected Weighted Centre Vertices $P(\bar{F}_s)$;
    Inner Slice Polygon $\Omega_s \equiv N \equiv A \cup B$;

Output:
    Maximal Circle $B_s(p, r)$;
1: $[ax := a_i(x), ay := a_i(y), az := a_i(z)] \in A, maxDist := 0.0$
2: **if** $(size(\bar{F}_s) < MaxCount_{radial})$ **then**
3:   **for** $i = -totalLoop$ to $totalLoop$ **do**
4:     **for** $j = -totalLoop$ to $totalLoop$ **do**
5:       The sampling range: $[bx := b_i(x), by := b_i(y), bz := b_i(z)] \in B$
6:       **for** $k = 0$ to $size(\bar{F}_s)$ **do**
7:         $minDist := 1.0 \times 10^{10}$
8:         Calculate dist = Distance(ax, ay, az, bx, by, bz)
9:         **if** $(dist < minDist))$ **then**
10:           minDist:= dist
11:         **end if**
12:       **end for**
13:       **if** $(maxDist < minDist))$ **then**
        Assign to Optimal Indices:

        $c_i := i$

        $c_j := j$
        $maxDist := minDist$
14:       **end if**
15:     **end for**
16:   **end for**
17: **end if**
18: **return** P

---

curvature, together with the projected angle and projected plane in the faces view and vertices view.

V. RESULTS AND DISCUSSION

The results generated by 3D-FSA can be seen in Fig. 15 and utilised by Jung *et al.* [50] in their morphological study of the femoral geometry, which focuses on the bowing and width among the Korean ethnicity for the age range between 20 and 89 years old [50], without the concern of any implant, deformity, or surgical history of the femur. There were a total of 1400 participants, of whom 2800 femurs were enrolled in the study.

The collected CT images of both femurs were fully scanned, and the conversion to 3D file formats was completed using a 3D modelling software. The 3D-FSA then reads the file and constructs a 3D femur. Next, 3D skeletonization was applied to obtain a compact representation of the femur, that is, its skeleton of the femur. Both the 3D femur and the skeleton were used to obtain the following parameters (together with the appropriate defined location) for the analysis of the femur shaft:

Algorithm 2 Algorithm for the Least Square Curvature Calculation

Input:
    Projected Weighted Centre Vertices $P(\bar{F}_s)$;
    Reprojected Weighted Centre Vertices $R[P(\bar{F}_s)]$;

Output:
    Curvature(κ);
1: *Reprojected Vertices*$(px, py, pz) \in R[P(\bar{F}_s)]$
2: $total = size(\bar{F}_s)$
3: **for** $i = 0$ to $total$ **do**
    $mx = \sum_{i=0}^{total} p_i x$
    $mz = \sum_{i=0}^{total} p_i z$
4: **end for**
5: Find the Mean for Both mx and my:

    $mx = \frac{mx}{size(\bar{F}_s)}, \quad mz = \frac{mz}{size(\bar{F}_s)}$
6: **for** $i = 0$ to $size(\bar{F}_s)$ **do**
    $tx_i = p_i x - mx$
    $tz_i = p_i z - mz$
7: **end for**
8: **for** $i = 0$ to $total$ **do**
    $x2 = (tx_i)^2; dx2 = \sum_{i=0}^{total} x2;$
    $dxz = \sum_{i=0}^{total} (tx_i \times tz_i)$
    $z2 = (tz_i)^2; dz2 = \sum_{i=0}^{total} z2$
9: **end for**
10: Reassign the Matrix Array

    $A[0] = dx2; A[1] = A[2] = dxz; A[2] = dz2$
11: Compute the Determinant –> det
12: Division with the Matrix Array A:

    $iA[0], iA[1], iA[2], iA[3]$
13: **for** $i = 0$ to $size(\bar{F}_s)$ **do**
    $ix_i = iA[0] \times tx_i + iA[1] \times tz_i$
    $iz_i = iA[2] \times tx_i + iA[3] \times tz_i$
    $iy_i = -\sum_{i=0}^{total} (dx2 + dz2)$
14: **end for**
15: **for** $i = 0$ to $size(\bar{F}_s)$ **do**
    $a0 = \sum_{i=0}^{total} ix_i \times iy_i; b0 = \sum_{i=0}^{total} iz_i \times iy_i$
16: **end for**
17: $a0 = \frac{a0}{2}; b0 = \frac{b0}{2}$
18: Calculate the Center: $x_i = a0 + mx; z_i = b0 + mz$
19: Calculate the Radius:

    $radius = \sqrt{dx2 + dz2 + a0^2 + b0^2}$
20: Calculate the Curvature (κ): $\frac{1}{radius}$
21: **return** *FILE*

The main three parameters are depicted in Fig. 16. To validate the measurement of 3D skeletonization, 50 participants who were evenly distributed by age and sex were selected to repeat the measurement after 2 months. Moreover, the intraclass correlation coefficient of each parameter was calculated, and the results showed that the 3D-FSA produced an
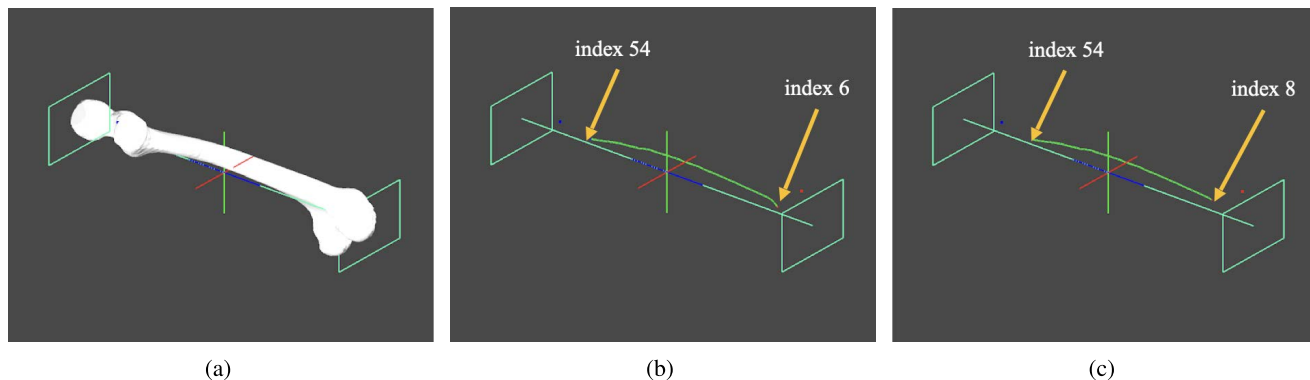
FIGURE 13. The involved range for the calculation of the minimum radius of curvature. (a) After the calculation of the maximum-minimum centre approach (Section IV-B), the results of 68 sliding windows are generated and displayed in faces view. (b) The results of the maximum-minimum centre approach are displayed in vertices view after the 'F' or 'f' key is pressed. Although 68 sliding windows are generated, only the indices from 6 (bottom margin is equal to 0.08%) to 54 (top margin is equal to 0.18%) are used to calculate the minimum radius of curvature. (c) Another example from the indices from 8 (bottom margin is equal to 0.11%) to 54 (top margin is equal to 0.18%) are used to calculate the minimum radius of curvature.
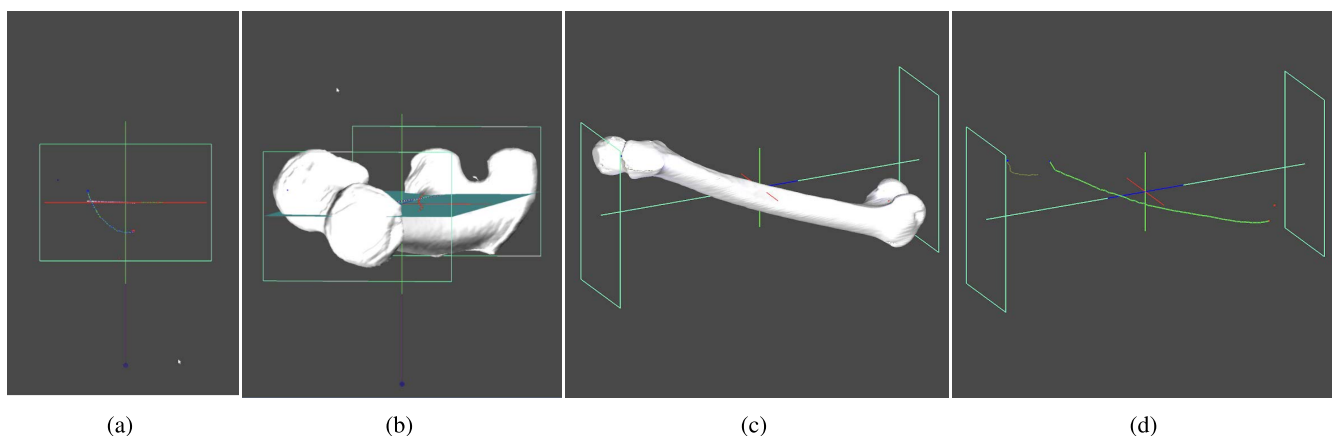
FIGURE 14. The projected vertices for the calculation of the minimum radius of curvature. (a) The projected angle of 0° to 180°. (b) Projected plane. (c) Resulting projection in faces view. (d) The resulting projection in vertices view.
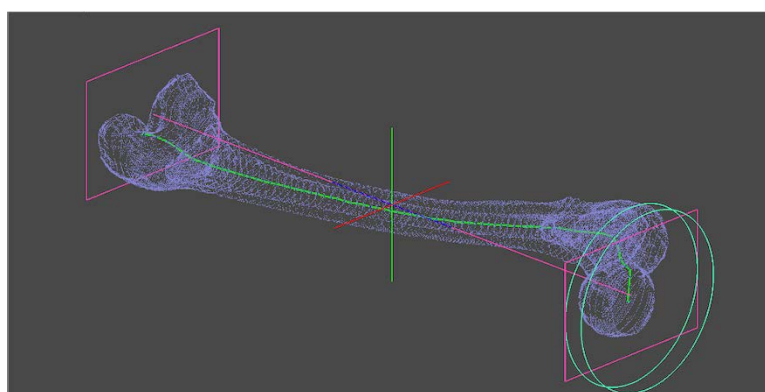

FIGURE 15. The 3D femur skeletonization result with the extension line of the weighted centre vertices (*green lines*).

accurate measurement compared with the two-dimensional measurement reproducible results [50].

This study also revealed that the age- and sex-related factors affected the femoral bowing and the diameter of the medullary canal. The results showed that women had more bowed femurs than did men. Moreover, as the age increased, the femur became more curved, and this tendency was more apparent in women. Consequently, these patients are more vulnerable to insufficiency fractures. Several studies [19], [33], [34], [37], [69], [70] have shown that Asians have a
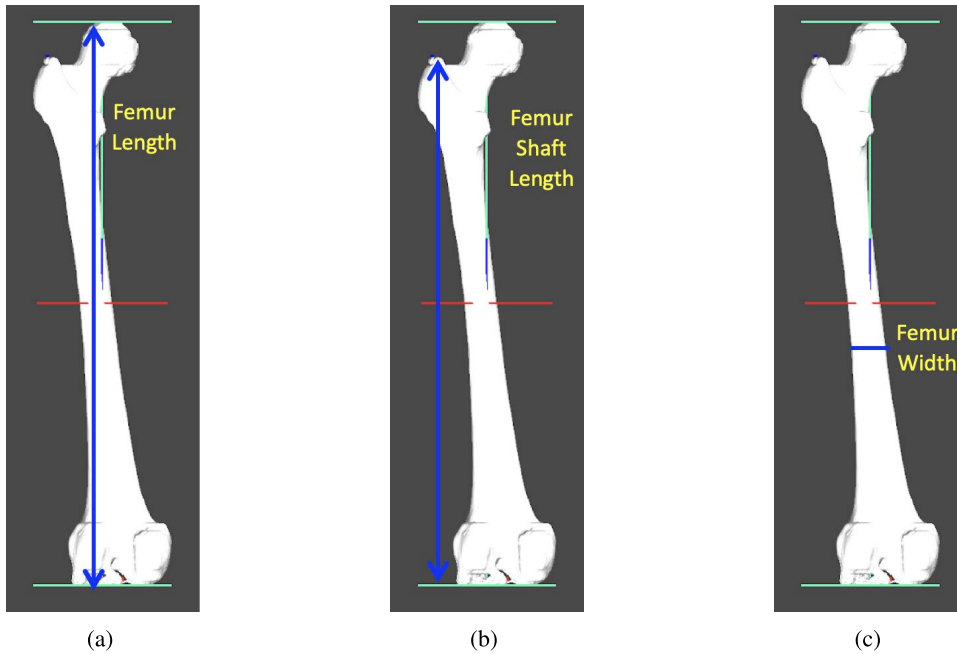
FIGURE 16. The obtained geometric parameters of the femur shaft. Left femur: (a) Femur length, (b) Femur shaft length, and (c) Femur width.

TABLE 1. Geometric Parameters and the Location of the Femur Shaft.

Parameters	Location (from)	Location (to)
Femur Length	Upper Pole of the Femoral Head	Bicondylar Baseline
Femur Shaft Length	Tip of the Greater Trochanter	Bicondylar Line
Narrowest Diameter of the Medullary Canal	Lesser Trochanter	Supracondylar Area
AP Length and Width of the Entire Femur	Lesser Trochanter	Supracondylar Area
Radius of Curvature (ROC) of the Femur	Lesser Trochanter	Supracondylar Area

smaller ROC than Caucasians, especially in women, and that femur bowing is correlated with race.

[21], [50] presumed that if 700 mm is the minimum ROC possible with the current nails, the current intramedullary nail would result in a mismatch problem in 11.5% of the Korean population because of their severely bowed femur. Their results demonstrated that during the ageing process, both the outer and internal diameter of the medullary canal were increased among women older than 50 years. Moreover, the linear regression analysis showed that femoral bowing was not related to medullary canal widening but was related to ageing rather than osteoporosis.

However, there are several limitations in the study as follows:

1) The collected data are not representative of each individual change, but rather of their ages.

   • The average height of men increased from 169 cm for those who were born after the Korean War in 1954 to 175 cm for those who were born in the year of 1983 [71].

   • [72] reported a good correlation between the rate of bone loss from a sample in a cross-sectional study and from longitudinal data over a 16-year of observational period.

2) The measured data did not have the resolution to assess cortical porosity or change because the images used were conventional CT images rather than micro-CT images.

To enhance the efficiency and accuracy of the 3D-FSA, 3D mesh segmentation and artificial intelligence (AI) techniques should be deployed with a sufficient amount of data. As created AI has globally-attributed to mostly one goal, it obtains a higher level of accuracy and surpasses the existing benchmarks. More data would result in better and more accurate models.

The 3D-FSA provides a great education platform for a better understanding of femur geometry. In addition, it provides a detailed guidance for the preparation and development of a new intramedullary nailing system.

VI. CONCLUSION

An automatic 3D-FSA based on the extracted skeleton of each individual patient was developed and used to provide an accurate 3D preoperative simulation. Moreover, 3D-FSA has provided an analysis platform for the geometry of the femoral shaft in assisting the morphological study that focuses on bowing and width among the Korean ethnicity for the age of 20 to 89 years old [50]. A total of 2800 femurs were enrolled in the study, and it was concluded that femoral bowing and the

width of the medullary canal gradually increased over time, especially among women. The results of these 3D analyses generated by the 3D-FSAs were accurate and reproducible. Therefore, this is the best reference for surgical preparation and implant designs.

REFERENCES

[1] A. M. Ghanem, A. H. Hamimi, J. R. Matta, A. Carass, R. M. Elgarf, A. M. Gharib, and K. Z. Abd-Elmoniem, "Automatic coronary wall and atherosclerotic plaque segmentation from 3D coronary CT angiography," *Sci. Rep.*, vol. 9, no. 1, pp. 1–13, Jan. 2019, doi: 10.1038/s41598-018-37168-4.

[2] J. Li, J. Weng, H. Xu, C. Zhou, D. Zhang, and G. Lu, "Design of robotic mannequin formed by flexible belt net," *Comput.-Aided Des.*, vol. 110, pp. 1–10, May 2019, doi: 10.1016/j.cad.2018.12.010.

[3] F. Buonamici, R. Furferi, L. Governi, S. Lazzeri, K. McGreevy, M. Servi, E. Talanti, F. Uchedd, and Y. Volpe, "A CAD-based procedure for designing 3D printable arm-wrist-hand cast," *Comput.-Aided Des. Appl.*, vol. 16, no. 1, pp. 25–34, Aug. 2018.

[4] C. Patruno, R. Marani, G. Cicirelli, E. Stella, and T. D'Orazio, "People re-identification using skeleton standard posture and color descriptors from RGB-D data," *Pattern Recognit.*, vol. 89, pp. 77–90, May 2019, doi: 10.1016/j.patcog.2019.01.003.

[5] A. C. Jalba, A. Sobiecki, and A. C. Telea, "An unified multiscale framework for planar, surface, and curve skeletonization," *IEEE Trans. Pattern Anal. Mach. Intell.*, vol. 38, no. 1, pp. 30–45, Jan. 2016, doi: 10.1109/TPAMI.2015.2414420.

[6] J. Cheng, X. Zheng, S. Chen, G. Liu, S. Xin, L. Lu, Y. Zhou, and C. Tu, "Skeletonization via dual of shape segmentation," *Comput. Aided Geometric Des.*, vol. 80, Jun. 2020, Art. no. 101856, doi: 10.1016/j.cagd.2020.101856.

[7] J. Tierny, J.-P. Vandeborre, and M. Daoudi, "Topology driven 3D mesh hierarchical segmentation," in *Proc. IEEE Int. Conf. Shape Modeling Appl. (SMI)*, Jun. 2007, pp. 215–220, doi: 10.1109/SMI.2007.38.

[8] C. Lin, L. Liu, C. Li, L. Kobbelt, B. Wang, S. Xin, and W. Wang, "SEGMAT: 3D shape segmentation using medial axis transform," *IEEE Trans. Vis. Comput. Graphics*, vol. 28, no. 6, pp. 2430–2444, Jun. 2022, doi: 10.1109/TVCG.2020.3032566.

[9] H. Blum, "A transformation for extracting new descriptors of shape," *Models Preception Speech Vis. Form*, vol. 19, no. 5, pp. 362–380, Nov. 1967.

[10] N. Amenta, S. Choi, and R. K. Kolluri, "The power crust, unions of balls, and the medial axis transform," *Comput. Geometry*, vol. 19, nos. 2–3, pp. 127–153, Jul. 2001, doi: 10.1016/S0925-7721(01)00017-7.

[11] K. Siddiqi, S. Bouix, A. Tannenbaum, and S. W. Zucker, "Hamilton-jacobi skeletons," *Int. J. Comput. Vis.*, vol. 48, no. 3, pp. 215–231, Jul. 2002, doi: 10.1023/A:1016376116653.

[12] A. Tabb and H. Medeiros, "Fast and robust curve skeletonization for real-world elongated objects," in *Proc. IEEE Winter Conf. Appl. Comput. Vis. (WACV)*, Mar. 2018, pp. 1935–1943, doi: 10.1109/WACV.2018.00214.

[13] Fact Sheet for Patients and Families. (Jul. 2012). *Open Reduction and Internal Fixation (ORIF)*. Intermountain Healthcare. [Online]. Available: https://intermountainhealthcare.org/ckr-ext/Dcmnt?ncid=521402750

[14] Y.-B. Gao, S.-L. Tong, J.-H. Yu, and W.-J. Lu, "[Case control study on open reduction internal fixation (ORIF) and minimally invasive percutaneous plate osteosynthesis (MIPPO) for the treatment of proximal humerus fractures in aged]," *Zhongguo Gu Shang China J. Orthopaedics Traumatol.*, vol. 28, no. 4, pp. 335–339, Apr. 2015. [Online]. Available: https://pubmed.ncbi.nlm.nih.gov/26072616/

[15] K. Nunez. *Repairing Major Bone Breaks With Open Reduction Internal Fixation Surgery*. Accessed: Mar. 24, 2022. [Online]. Available: https://www.healthline.com/health/orif-surgery

[16] WebMD. *What is ORIF Surgery*. Accessed: Mar. 24, 2022. [Online]. Available: https://www.webmd.com

[17] M. R. Bong, F. J. Kummer, K. J. Koval, and K. A. Egol, "Intramedullary nailing of the lower extremity: Biomechanics and biology," *J. Amer. Acad. Orthopaedic Surgeons*, vol. 15, no. 2, pp. 97–106, Feb. 2007.

[18] OrthoInfo. *Femur Shaft Fractures (Broken Thighbone)*. Accessed: Mar. 24, 2022. [Online]. Available: https://orthoinfo.aaos.org/en/diseases–conditions/femur-shaft-fracture%s-broken-thighbone/

[19] K. A. Egol, E. Y. Chang, J. Cvitkovic, F. J. Kummer, and K. J. Koval, "Mismatch of current intramedullary nails with the anterior bow of the femur," *J. Orthopaedic Trauma*, vol. 18, no. 7, pp. 410–415, Aug. 2004.

[20] W. Chan, C. Yen, K. Wong, P. Tse, and K. Mak, "Breakage of intramedullary femoral guide rod during total knee arthroplasty: A case report," *J. Orthopaedic Surgery*, vol. 14, no. 1, pp. 96–98, Apr. 2006, doi: 10.1177/230949900601400121.

[21] J. H. Park, Y. Lee, O.-J. Shon, H. C. Shon, and J. W. Kim, "Surgical tips of intramedullary nailing in severely bowed femurs in atypical femur fractures: Simulation with 3D printed model," *Injury*, vol. 47, no. 6, pp. 1318–1324, Jun. 2016, doi: 10.1016/j.injury.2016.02.026.

[22] J. W. Kim, H. Kim, C.-W. Oh, J.-W. Kim, O.-J. Shon, Y.-S. Byun, J. J. Kim, H. K. Oh, H. Minehara, K.-T. Hwang, and K. C. Park, "Surgical outcomes of intramedullary nailing for diaphyseal atypical femur fractures: Is it safe to modify a nail entry in bowed femur?" *Arch. Orthopaedic Trauma Surg.*, vol. 137, no. 11, pp. 1515–1522, Aug. 2017, doi: 10.1007/s00402-017-2764-1.

[23] J.-W. Kim, C.-W. Oh, J.-K. Oh, K.-H. Park, H.-J. Kim, T.-S. Kim, I. Seo, and E.-K. Park, "Treatment of infra-isthmal femoral fracture with an intramedullary nail: Is retrograde nailing a better option than antegrade nailing?" *Arch. Orthopaedic Trauma Surg.*, vol. 138, no. 9, pp. 1241–1247, May 2018, doi: 10.1007/s00402-018-2961-6.

[24] I. Hudson, K. Mauch, M. Schuurman, M. T. Padela, P. Gheraibeh, and R. Vaidya, "Effect of inherent tibial asymmetry on leg length discrepancy measurements after intramedullary nailing of comminuted femoral shaft fractures," *SICOT-J*, vol. 5, p. 1, Jan. 2019, doi: 10.1051/sicotj/2018053.

[25] S. Sabharwal, C. Zhao, J. J. McKeon, E. McClemens, M. Edgar, and F. Behrens, "Computed radiographic measurement of limb-length discrepancy: Full-length standing anteroposterior radiograph compared with scanogram," *JBJS*, vol. 88, no. 10, pp. 2243–2251, Oct. 2006, doi: 10.2106/JBJS.E.01179.

[26] S. Sabharwal, C. Zhao, J. McKeon, T. Melaghari, M. Blacksin, and C. Wenekor, "Reliability analysis for radiographic measurement of limb length discrepancy: Full-length standing anteroposterior radiograph versus scanogram," *J. Pediatric Orthopaedics*, vol. 27, no. 1, pp. 46–50, Jan. 2007, doi: 10.1097/01.bpo.0000242444.26929.9f.

[27] S. Sabharwal and A. Kumar, "Methods for assessing leg length discrepancy," *Clin. Orthopaedics Rel. Res.*, vol. 466, no. 12, pp. 2910–2922, Dec. 2008, doi: 10.1007/s11999-008-0524-9.

[28] A. Aaron, D. Weinstein, D. Thickman, and R. Eilert, "Comparison of orthoroentgenography and computed tomography in the measurement of limb-length discrepancy," *J. Bone Joint Surg.*, vol. 74, no. 6, pp. 897–902, Jul. 1992.

[29] R. Vaidya, B. Anderson, A. Elbanna, R. Colen, D. Hoard, and A. Sethi, "CT scanogram for limb length discrepancy in comminuted femoral shaft fractures following IM nailing," *Injury*, vol. 43, no. 7, pp. 1176–1181, Jul. 2012, doi: 10.1016/j.injury.2012.03.022.

[30] D. Herscovici and J. M. Scaduto, "Assessing leg length after fixation of comminuted femur fractures," *Clin. Orthopaedics Rel. Res.*, vol. 472, no. 9, pp. 2745–2750, Sep. 2014, doi: 10.1007/s11999-013-3292-0.

[31] D.-I. Kim, D.-S. Kwak, and S.-H. Han, "Sex determination using discriminant analysis of the medial and lateral condyles of the femur in Koreans," *Forensic Sci. Int.*, vol. 233, nos. 1–3, pp. 121–125, Dec. 2013, doi: 10.1016/j.forsciint.2013.08.028.

[32] H.-J. Cho, D.-S. Kwak, and I.-B. Kim, "Morphometric evaluation of Korean femurs by geometric computation: Comparisons of the sex and the population," *BioMed Res. Int.*, vol. 2015, pp. 1–9, Aug. 2015, doi: 10.1155/2015/730538.

[33] X.-Y. Su, J.-X. Zhao, Z. Zhao, L.-C. Zhang, C. Li, J.-T. Li, J.-F. Zhou, L.-H. Zhang, and P.-F. Tang, "Three-dimensional analysis of the characteristics of the femoral canal isthmus: An anatomical study," *BioMed Res. Int.*, vol. 2015, pp. 1–9, Jun. 2015, doi: 10.1155/2015/459612.

[34] A. H. K. Abdelaal, N. Yamamoto, K. Hayashi, A. Takeuchi, A. F. Morsy, S. Miwa, Y. Kajino, D. A. Rubio, and H. Tsuchiya, "Radiological assessment of the femoral bowing in Japanese population," *SICOT-J*, vol. 2, p. 2, Jan. 2016, doi: 10.1051/sicotj/2015037.

[35] J. N. Insall, R. Binazzi, M. Soudry, and L. A. Mestriner, "Total knee arthroplasty," *Clin. Orthopaedics Related Research*, vol. 192, pp. 13–22, Jan. 1985.

[36] M. A. Ritter, P. M. Faris, E. M. Keating, and J. B. Meding, "Postoperative alignment of total knee replacement. Its effect on survival," *Clin. Orthopaedics Related Res.*, vol. 299, pp. 153–156, Feb. 1994.

[37] M. B. Trudell, "Anterior femoral curvature revisited: Race assessment from the femur," *J. Forensic Sci.*, vol. 44, no. 4, pp. 700–707, 1999.

[38] I. Papaioannou, G. Pantazidou, A. Baikousis, and P. Korovessis, "Femoral bowing and femoral neck-shaft angle evaluation can reduce atypical femoral fractures in osteoporotic patients: A scientific report," *Cureus*, vol. 12, no. 10, pp. 1–5, Oct. 2020, doi: 10.7759/cureus.10771.

[39] W. Bruns, M. Bruce, G. Prescott, and N. Maffulli, "Temporal trends in femoral curvature and length in medieval and modern Scotland," *Amer. J. Phys. Anthropol.*, vol. 119, no. 3, pp. 224–230, Oct. 2002, doi: 10.1002/ajpa.10113.

[40] I. De Groote, "Femoral curvature in neanderthals and modern humans: A 3D geometric morphometric analysis," *J. Hum. Evol.*, vol. 60, no. 5, pp. 540–548, May 2011, doi: 10.1016/j.jhevol.2010.09.009.

[41] P. C. Noble, J. W. Alexander, L. J. Lindahl, D. T. Yew, W. M. Granberry, and H. S. Tullos, "The anatomic basis of femoral component design," *Clin. Orthopaedics Related Res.*, vol. 235, pp. 148–165, Oct. 1988.

[42] A. Harma, B. Germen, H. M. Karakas, N. Elmali, and M. Inan, "The comparison of femoral curves and curves of contemporary intramedullary nails," *Surgical Radiol. Anatomy*, vol. 27, no. 6, pp. 502–506, Aug. 2005, doi: 10.1007/s00276-005-0019-2.

[43] K. P. Walsh, J. R. Fowler, O. Chen, J. P. Gaughan, S. Ali, M. Rehman, and S. Rehman, "The validity and reliability of preoperative radiographic canal diameter measurements of the femur," *HSS J.*, vol. 9, no. 2, pp. 150–156, Jul. 2013, doi: 10.1007/s11420-013-9334-z.

[44] P. Rubin, P. Leyvraz, J. Aubaniac, J. Argenson, P. Esteve, and B. de Roguin, "The morphology of the proximal femur. A three-dimensional radiographic analysis," *J. Bone Joint Surg. Brit. Volume*, vols. 74–B, no. 1, pp. 28–32, Jan. 1992, doi: 10.1302/0301-620X.74B1.1732260.

[45] H. Laine, K. Kontola, M. Lehto, M. Pitkänen, P. Jarske, and T. Lindholm, "Image processing for femoral endosteal anatomy detection: Description and testing of a computed tomography based program," *Phys. Med. Biol.*, vol. 42, no. 4, p. 673, 1997.

[46] B. Yang, J.-K. Yu, Z.-Z. Zheng, Z.-H. Lu, and J.-Y. Zhang, "Comparative study of sex differences in distal femur morphology in osteoarthritic knees in a Chinese population," *PLoS ONE*, vol. 9, no. 2, Feb. 2014, Art. no. e89394, doi: 10.1371/journal.pone.0089394.

[47] M. Y. Baharuddin, S.-H. Salleh, A. H. Zulkifly, M. H. Lee, and A. M. Noor, "Morphological study of the newly designed cementless femoral stem," *BioMed Res. Int.*, vol. 2014, pp. 1–11, Jun. 2014, doi: 10.1155/2014/692328.

[48] M. Masjedi, C. Tay, S. J. Harris, and J. P. Cobb, "A local reference frame for describing the proximal human femur: Application in clinical settings," *Skeletal Radiol.*, vol. 43, no. 3, pp. 323–329, Mar. 2014, doi: 10.1007/s00256-013-1782-5.

[49] J.-X. Zhao, X.-Y. Su, Z. Zhao, L.-C. Zhang, Z. Mao, H. Zhang, L.-H. Zhang, and P.-F. Tang, "Predicting the optimal entry point for femoral antegrade nailing using a new measurement approach," *Int. J. Comput. Assist. Radiol. Surg.*, vol. 10, no. 10, pp. 1557–1565, Oct. 2015, doi: 10.1007/s11548-015-1182-5.

[50] I. J. Jung, E. J. Choi, B. G. Lee, and J. W. Kim, "Population-based, three-dimensional analysis of age- and sex-related femur shaft geometry differences," *Osteoporosis Int.*, vol. 32, no. 8, pp. 1631–1638, Aug. 2021, doi: 10.1007/s00198-021-05841-6.

[51] L.-P. Chen, T.-K. Chang, T.-Y. Huang, T.-G. Kwok, and Y.-C. Lu, "The correlation between lateral bowing angle of the femur and the location of atypical femur fractures," *Calcified Tissue Int.*, vol. 95, no. 3, pp. 240–247, Jul. 2014, doi: 10.1007/s00223-014-9887-y.

[52] H. Yoo, Y. Cho, Y. Park, and S. Ha, "Lateral femoral bowing and the location of atypical femoral fractures," *Hip Pelvis*, vol. 29, no. 2, pp. 127–132, Jun. 2017, doi: 10.5371/hp.2017.29.2.127.

[53] K. Atesok, D. Galos, L. M. Jazrawi, and K. A. Egol, "Preoperative planning in orthopaedic surgery: Current practice and evolving applications," *Bull. Nyu Hospital Joint Diseases*, vol. 73, no. 4, p. 257, Oct. 2015.

[54] S. K. Coreline. *AVIEW Modeler; Coreline Soft*. Accessed: Mar. 28, 2022. [Online]. Available: https://www.corelinesoft.com/home-eng-2/

[55] D. Chakravorty. *Obj File Format—All You need to Know*. Accessed: Jan. 20, 2019. [Online]. Available: https://all3dp.com/1/obj-file-format-3d-printing-cad/

[56] H. I. Choi, S. W. Choi, and H. P. Moon, "Mathematical theory of medial axis transform," *Pacific J. Math.*, vol. 181, no. 1, pp. 57–88, 1997, doi: 10.2140/pjm.1997.181.57.

[57] F. Eyüboglu, C. Sayacaa, M. Çalik, D. Korkem, L. N. Tascilar, and D. Kaya, "Kinesiology of the hip," in *Comparative Kinesiology of the Human Body*, S. Angin and I. E. Simsek, Eds. New York, NY, USA: Academic, 2020, pp. 375–392.

[58] P. Lindstrom and G. Turk, "Evaluation of memoryless simplification," *IEEE Trans. Vis. Comput. Graphics*, vol. 5, no. 2, pp. 98–115, Apr. 1999, doi: 10.1109/2945.773803.

[59] J.-Y. Ru, L.-X. Chen, F.-Y. Hu, D. Shi, R. Xu, J.-W. Du, and Y.-F. Niu, "Factors associated with development of re-nonunion after primary revision in femoral shaft nonunion subsequent to failed intramedullary nailing," *J. Orthopaedic Surg. Res.*, vol. 13, no. 1, pp. 1–11, Jul. 2018, doi: 10.1186/s13018-018-0886-y.

[60] R. Jain, R. Kasturi, and B. G. Schunk, *Machine Vision*. New Delhi, India: Indo American Books, 2016.

[61] M. Khurma. (2013). *Radius of Curvature Formula*. Accessed: Apr. 11, 2022. [Online]. Available: https://www.cuemath.com/radius-of-curvature-formula/

[62] W. L. Jungers, L. R. Godfrey, E. L. Simons, and P. S. Chatrath, "Phalangeal curvature and positional behavior in extinct sloth lemurs (primates, Palaeopropithecidae)," *Proc. Nat. Acad. Sci. USA*, vol. 94, no. 22, pp. 11998–12001, Oct. 1997, doi: 10.1073/pnas.94.22.11998.

[63] T. Gausepohl, D. Pennig, J. Koebke, and S. Harnoss, "Antegrade femoral nailing: An anatomical determination of the correct entry point," *Injury*, vol. 33, no. 8, pp. 701–705, Oct. 2002, doi: 10.1016/S0020-1383(02)00158-4.

[64] K. Subburaj, B. Ravi, and M. Agarwal, "Computer-aided methods for assessing lower limb deformities in orthopaedic surgery planning," *Computerized Med. Imag. Graph.*, vol. 34, no. 4, pp. 277–288, Jun. 2010, doi: 10.1016/j.compmedimag.2009.11.003.

[65] Y. Oh, Y. Wakabayashi, Y. Kurosa, M. Ishizuki, and A. Okawa, "Stress fracture of the bowed femoral shaft is another cause of atypical femoral fracture in elderly japanese: A case series," *J. Orthopaedic Sci.*, vol. 19, no. 4, pp. 579–586, Jul. 2014, doi: 10.1007/s00776-014-0572-9.

[66] J. Maratt, P. L. Schilling, S. Holcombe, R. Dougherty, R. Murphy, S. C. Wang, and J. A. Goulet, "Variation in the femoral bow: A novel high-throughput analysis of 3922 femurs on cross-sectional imaging," *J. Orthopaedic Trauma*, vol. 28, no. 1, pp. 6–9, Jan. 2014, doi: 10.1097/BOT.0b013e31829ff3c9.

[67] A. J. Fantry, G. Elia, B. G. Vopat, and A. H. Daniels, "Distal femoral complications following antegrade intramedullary nail placement," *Orthopedic Rev.*, vol. 7, no. 1, pp. 12–14, Mar. 2015, doi: 10.4081/or.2015.5820.

[68] A. Shetty, P. M. Shenoy, and R. Swaminathan, "Mismatch of long gamma intramedullary nail with bow of the femur: Does radius of curvature of the nail increase risk of distal femoral complications?" *J. Clin. Orthopaedics Trauma*, vol. 10, no. 2, pp. 302–304, Mar. 2019, doi: 10.1016/j.jcot.2017.12.006.

[69] H. Tsuchie, N. Miyakoshi, Y. Kasukawa, S. Senma, Y. Narita, S. Miyamoto, Y. Hatakeyama, K. Sasaki, and Y. Shimada, "Factors related to curved femur in elderly Japanese women," *Upsala J. Med. Sci.*, vol. 121, no. 3, pp. 170–173, May 2016, doi: 10.1080/03009734.2016.1185200.

[70] D. M. Thiesen, F. Prange, J. Berger-Groch, D. Ntalos, A. Petersik, B. Hofstätter, J. M. Rueger, T. O. Klatte, and M. J. Hartel, "Femoral antecurvation—A 3D CT analysis of 1232 adult femurs," *PLoS ONE*, vol. 13, no. 10, Oct. 2018, Art. no. e0204961, doi: 10.1371/journal.pone.0204961.

[71] D. Schwekendiek and J. Seong-Ho, "From the poorest to the tallest in East Asia: The secular trend in height of South Koreans," *Korea J.*, vol. 50, no. 3, pp. 151–175, Sep. 2010.

[72] L. J. Melton, E. J. Atkinson, M. K. O'Connor, W. M. O'Fallon, and B. L. Riggs, "Determinants of bone loss from the femoral neck in women of different ages," *J. Bone Mineral Res.*, vol. 15, no. 1, pp. 24–31, Jan. 2000.

SEOW HUI SAW received the B.I.T. degree in software engineering from Multimedia University, Malaysia, and the M.Eng. degree in software engineering from Dongseo University, South Korea. She is currently pursuing the Ph.D. degree with the Department of Computer Science (DCS), Faculty of Information and Communication Technology (FICT), University of Tunku Abdul Rahman (UTAR), Kampar, Perak.

She is also a Faculty Member at the DCS, FICT, UTAR. She has supervised a number of undergraduates in this area and won a couple of awards in the faculty final year project (FYP) competitions. Several of her FYP students winning demos were collected to show in UTAR open day to attract more high school students to join UTAR. Moreover, she was elected as a Finalist of the Ministry of Education, Culture, Sports, Science and Technology, Japan (MEXT) Scholarship Program to join a research group at The University of Tokyo, in April 2007, for a period of four years. Since then, she has conducted research activities on graph visualization and 3D mesh modeling. Her research interests include computer graphics (CG), computer graphics and interactivity, which includes augmented reality (AR) and virtual reality (VR), visualization and multimedia, and 3D mesh processing and optimization.

BYUNG-GOOK LEE received the B.S. degree in mathematics from Yonsei University, in 1987, and the M.S. and the Ph.D. degrees in applied mathematics from the Korea Advanced Institute of Science and Technology (KAIST), South Korea, in 1989 and 1993, respectively. From 1993 to 1995, he worked as a Senior Engineer with DACOM Corporation Research and Development Center. Since 1995, he has been with Dongseo University, South Korea, where he is currently a Professor with the Division of Computer and Information Engineering. His research interests include computer-aided geometric modeling, computer graphics, image processing, computer vision, and deep learning.

HONG TAT EWE (Senior Member, IEEE) received the Bachelor of Engineering degree(Hons.) in electrical engineering from the University of Malaya, Malaysia, the Masters of Science degree in electrical engineering and computer science from the MIT, USA, and the Ph.D. degree from Multimedia University, Malaysia.

He had worked before with Motorola Penang, Intel Penang, MIT's Research Laboratory for Electronics, University of Malaya, and Multimedia University (MMU), where his last position held in MMU was the Vice President (academic). He is currently a Senior Professor with the Lee Kong Chian Faculty of Engineering and Science and the President/CEO of the Universiti Tunku Abdul Rahman (UTAR). He has authored or coauthored books, international journals and conferences, and newspaper column articles. His research interests include microwave remote sensing, satellite image processing, wireless sensor networks, and intelligent computing. He is also active in consultancy and technopreneurship development works and has been a consultant for several listed and startup companies in Malaysia.

Dr. Ewe is a fellow of the Academy of Sciences Malaysia (ASM) and a fellow and the Secretary General of the ASEAN Academy of Engineering and Technology (AAET). He was a recipient of a number of awards, including The Young Scientist Award of URSI (International Union of Radio Science) in 1996, The Outstanding Young Malaysian (TOYM) Award 2005 for Academic Leadership and Accomplishment, and The Toray Science and Technology Award by the Malaysian Toray Science Foundation in 2011. He is the Chair of the IEEE Geoscience and Remote Sensing Society Malaysia Chapter, the Chairperson of Science, Technology and Innovations Committee of ACCCIM, the Educational Counselor and a Regional Chair (Malaysia) of the MIT Educational Council, and was a Council Member of the Malaysia Qualifications Agency (MQA), from 2013 to 2018.

$\bullet \bullet \bullet$